

Strongly momentum-dependent screening dynamics in $\text{La}_{0.5}\text{Sr}_{1.5}\text{MnO}_4$ observed with resonant inelastic x-ray scattering

X. Liu,^{1,2} T. F. Seman,³ K. H. Ahn,³ Michel van Veenendaal,^{4,5} D. Casa,⁴ D. Prabhakaran,⁶ A. T. Boothroyd,⁶ H. Ding,² and J. P. Hill¹

¹Condensed Matter Physics and Materials Science Department, Brookhaven National Laboratory, Upton, New York 11973, USA

²Beijing National Laboratory for Condensed Matter Physics, and Institute of Physics, Chinese Academy of Sciences, Beijing 100190, China

³Department of Physics, New Jersey Institute of Technology, Newark, New Jersey 07102, USA

⁴Advanced Photon Source, Argonne National Laboratory, Argonne, Illinois 60439, USA

⁵Department of Physics, Northern Illinois University, De Kalb, Illinois 60115, USA

⁶Department of Physics, University of Oxford, Clarendon Laboratory, Parks Road, Oxford OX1 3PU, United Kingdom

(Received 24 October 2012; revised manuscript received 3 May 2013; published 14 May 2013)

We report strongly momentum-dependent short-ranged charge screening dynamics in CE-type charge, orbital, and spin ordered $\text{La}_{0.5}\text{Sr}_{1.5}\text{MnO}_4$, based on Mn *K*-edge resonant inelastic x-ray scattering data. Through a comparison with theoretical calculations, we show that the observed momentum dependence reflects highly localized, nearest-neighbor screening of the transient local charge perturbation in this compound with an excitonlike screening cloud, rather than delocalized screening. The size of the screening cloud is estimated to be about 0.4–0.5 interatomic distances.

DOI: [10.1103/PhysRevB.87.201103](https://doi.org/10.1103/PhysRevB.87.201103)

PACS number(s): 78.70.Ck, 71.27.+a, 75.47.Lx, 78.70.Dm

The response of a strongly correlated electron system to a sizable, localized potential is highly nontrivial,^{1,2} and yet of fundamental importance. It lies at the heart of any understanding of the role of dopant ions, the primary means of controlling the phase behavior of many such systems. Such dopants affect the material properties in complex ways, in addition to introducing carriers, and have been directly correlated with electronic inhomogeneities^{3,4} and shown to induce local spin polarization even when nonmagnetic.⁵ However, the understanding of dopant-induced phenomena is poor, mainly because the full calculation of the electronic response to such a perturbation remains a defining challenge in many-body physics, even for the homogeneous electron gas,⁶ let alone for strongly correlated systems.

Among many theoretical attempts to model the dopant problem,^{7–10} perhaps the most straightforward is to treat the dopant simply as a localized potential. One may achieve a similar situation experimentally by creating a deep core hole on a given site. Such a core hole has a potential of a few eV, similar in size to that from a dopant. The question is, can one measure the response of the system to this perturbation, that is, measure the associated screening dynamics of the core hole?

K-edge resonant inelastic x-ray scattering (RIXS)^{11,12} offers the possibility of doing just this in *3d* transition metal compounds. This technique has been mostly discussed in the limit of a strong or weak core-hole potential (U_{core}) relative to the bandwidth.¹³ In such cases, the intermediate states screening the transient core hole can be integrated out and the RIXS response is directly related to the dynamic structure factor. However, when U_{core} is comparable to the bandwidth, as is typical for *3d* transition metal compounds, the screening is more complicated because there is an asymmetry between the electron and hole excitations. Rather than being integrated out, the intermediate states then become important in determining the RIXS response.¹² This offers the intriguing possibility of projecting the screening related to such a core hole onto the valence band excitations. This in turn would allow the size

and shape of the screening cloud to be determined, and its relationship to the electronic structure to be explored.

In this Rapid Communication, we report *K*-edge RIXS measurements of the momentum and energy dependence of the screening dynamics for a transient local potential in the half-doped manganite, $\text{La}_{0.5}\text{Sr}_{1.5}\text{MnO}_4$, in its charge, orbital, and spin ordered state. We find strong momentum dependence of the intensity of the across-gap excitation, with a dramatic increase on moving away from the two-dimensional (2D) zone center. We show that this behavior reflects the size and shape of the real-space screening cloud and demonstrate that in $\text{La}_{0.5}\text{Sr}_{1.5}\text{MnO}_4$ the screening distance is very short, with a screening cloud of about 0.4–0.5 interatomic distances in size.

A single crystal of $\text{La}_{0.5}\text{Sr}_{1.5}\text{MnO}_4$ was grown by the traveling solvent floating zone method. It has a tetragonal structure at room temperature with *I4/mmm* symmetry and undergoes a charge and orbital ordering transition around 230 K, accompanied by complex structural distortions.¹⁴ For simplicity, we use here the *I4/mmm* notation throughout. The wave vectors of the charge and orbital ordering are then of the form $(\frac{1}{2}, \frac{1}{2}, L)$ and $(\frac{1}{4}, \frac{1}{4}, L)$, respectively. In the low temperature ordered state, $\text{La}_{0.5}\text{Sr}_{1.5}\text{MnO}_4$ is an insulator with a large gap between the e_g states.¹⁵ The behavior of the excitation between these predominantly Mn *3d* states, labeled as a *d-d* transition, is the focus of this study. The Mn *K*-edge RIXS experiments were performed at Advanced Photon Source on beamlines 30-ID and 9-ID with an instrumental energy resolution of about 270 meV [full width at half maximum (FWHM)]. The polarization dependence of the RIXS process is controlled by placing the [001] and [110] directions of the crystal in the scattering plane. The incident beam polarization is perpendicular to the scattering plane, i.e., parallel to the $[1\bar{1}0]$ direction. Thus the incident polarization condition is fixed for all the $\mathbf{Q} = (H, H, L)$ points surveyed. All the data presented were collected at $T = 20$ K. Data are normalized by incident beam intensity and corrected for footprint variations.

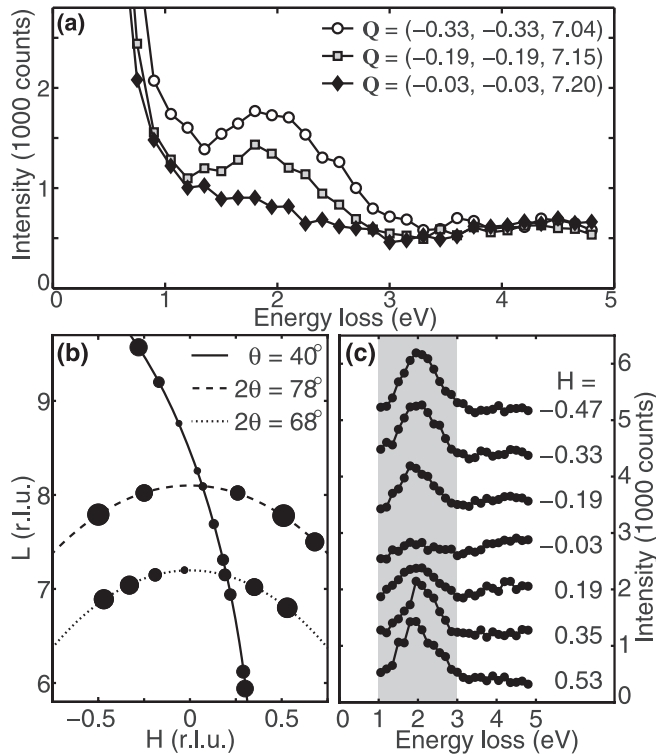


FIG. 1. (a) RIXS spectra at three \mathbf{Q} points. (b) The \mathbf{Q} points surveyed in the (H, H, L) plane. The radius of the dot is proportional to the integrated intensity of the 2 eV peaks. θ and 2θ are the incident and detector angles. (c) RIXS spectra for the \mathbf{Q} points along the $2\theta = 68^\circ$ line, with the elastic intensity subtracted. The gray shaded region is the energy window used in calculating the integrated intensity of the feature.

In Fig. 1(a), we show RIXS spectra taken at three \mathbf{Q} points. In each case, there is a large elastic line centered at zero energy loss. The d - d transition appears as a peak on the tail of the elastic scattering at around 2 eV, consistent with optics,¹⁶ electron-energy-loss spectroscopy (EELS),¹⁷ and other K -edge RIXS observations.^{18,19} Remarkably, the RIXS spectra show a strong momentum dependence of the intensity of this feature. At $\mathbf{Q}_0 = (-0.03, -0.03, 7.20)$ with very small in-plane momentum transfer, the 2 eV peak is almost unobservable. This momentum dependence is confirmed with RIXS spectra collected at a large number of \mathbf{Q} points, as shown in Figs. 1(b) and 1(c). To control the systematics resulting from polarization factors, the data were taken either at fixed sample angle θ or fixed detector angle 2θ . In all cases, the incident polarization is parallel to the $[1\bar{1}0]$ direction. With the detector position 2θ fixed, polarization effects associated with the outgoing x ray are eliminated. Figure 1(c) shows RIXS spectra with the elastic line subtracted²⁰ for the \mathbf{Q} points with $2\theta = 68^\circ$. We take the integrated intensity $I(\mathbf{Q})$ over the 1–3 eV range as a measure of the strength of the 2 eV peak. The size of the symbols in Fig. 1(b) is proportional to $I(\mathbf{Q})$. A clear systematic dependence on momentum transfer is observed.

The integrated intensities of the d - d excitation are plotted as a function of the in-plane momentum transfer in Fig. 2(b). In order to quantitatively compare the experimental data with the theoretical calculations (discussed below), the

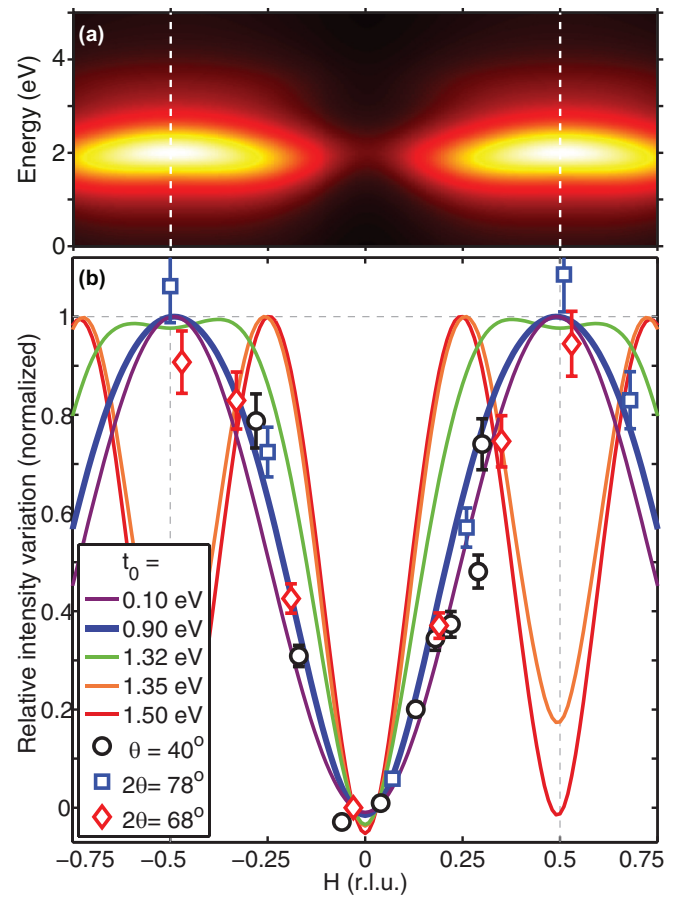


FIG. 2. (Color online) (a) Contour plot of RIXS intensity calculated for the electron hopping parameter $t_0 = 0.9$ eV, after averaging over twin domains. (b) The integrated RIXS intensity of the 2 eV peak relative to the $(-0.03, -0.03)$ point, plotted with respect to the in-plane momentum transfer along the (H, H) direction. Symbols represent experimental data. Lines represent theoretical results for different values of t_0 . Both experimental data and theoretical results are normalized for comparison.

integrated intensities are plotted relative to the intensity at $\mathbf{Q}_0 = (-0.03, -0.03, 7.20)$,²¹ i.e., $I(\mathbf{Q}) - I(\mathbf{Q}_0)$. This removes the uncertainty in determining the common background for all \mathbf{Q} points. The strength of the 2 eV d - d excitation exhibits a minimum at zero in-plane momentum transfer and a maximum at $(0.5, 0.5, L)$. Interestingly, although there is a large variation in the L values for the various \mathbf{Q} points [see Fig. 1(b)], all the measurements collapse onto a single curve in Fig. 2(b). This demonstrates that there is negligible L dependence to this behavior, consistent with the 2D nature of this single layered manganite. Further, it implies that the polarization factors are indeed constant for our experimental geometry. From here on, the momentum transfer will be denoted simply as $\mathbf{Q}_{2D} = (H, H)$.

The experimental data in Figs. 1 and 2 show our main experimental observations. The across-gap d - d excitation in $\text{La}_{0.5}\text{Sr}_{1.5}\text{MnO}_4$, as observed by RIXS, exhibits a strong momentum dependence. While the position of the peak shows no appreciable dispersion, the intensity increases rapidly as the in-plane momentum transfer increases away from the 2D zone center. Near the zone center, the spectral weight

of the 2 eV feature almost disappears. This is a surprising result. The disappearance of this RIXS spectral weight cannot be the result of the dynamic structure factor going to zero, since this feature is observed in the optical response,¹⁶ which probes the zero momentum transfer response function. This demonstrates that *K*-edge RIXS in $\text{La}_{0.5}\text{Sr}_{1.5}\text{MnO}_4$ is indeed in the intermediate core-hole potential regime, discussed above. In the following, we detail this momentum dependence and show that it arises from the intermediate state screening dynamics and in particular that it reflects the real-space extent of the screening cloud.

To understand this strong in-plane momentum dependence, we calculated the RIXS response from $\text{La}_{0.5}\text{Sr}_{1.5}\text{MnO}_4$ for a two-dimensional 16×16 Mn cluster with periodic boundary conditions. The initial and final states of the unperturbed system, and the intermediate states in the presence of the 1s core-hole on-site Coulomb potential, are solved numerically with a tight-binding approach. The Hamiltonian employed is similar to the one in Ref. 22, which includes the nearest-neighbor electron hopping within the MnO_2 plane, the Jahn-Teller and isotropic electron-lattice coupling, the Hund's coupling to the CE-type ordered t_{2g} spins, and the Coulomb interaction between e_g electrons within the Hartree-Fock approximation.²³ The sizes of the distortions of the oxygen octahedra are taken from Ref. 14. The RIXS spectra are then calculated from the Kramers-Heisenberg formula,^{11,12}

$$I \propto \sum_f \left| \sum_n \frac{\langle f | \mathcal{D}^\dagger | n \rangle \langle n | \mathcal{D} | g \rangle}{E_g + \hbar\omega_{\mathbf{k}} - E_n + i\Gamma_n} \right|^2 \delta(E_f - E_g - \hbar\Delta\omega), \quad (1)$$

where $|f\rangle$, $|n\rangle$, and $|g\rangle$ represent the final, intermediate, and initial states, and E_f , E_n , and E_g their energies. Γ_n is the inverse of the intermediate state lifetime, and \mathcal{D}^\dagger and \mathcal{D} are the RIXS dipole transition operators. $\hbar\omega_{\mathbf{k}}$ and $\hbar\Delta\omega$ are the incident x-ray energy and the energy loss, respectively. The calculated RIXS intensity is averaged over configurations in which the zigzag chains of orbital order are along either the $[110]$ or the $[\bar{1}\bar{1}0]$ directions, to take into account twinning effects in real crystals. Details of the calculation will be published elsewhere.

The calculated RIXS spectra were found to be most sensitive to the e_g - e_g hybridization and the coupling of the e_g electrons to the distortions of oxygen octahedra. These two effects are parametrized as t_0 and λ in our Hamiltonian, where t_0 is the hopping between $3x^2-r^2$ orbitals along the x direction and λ is proportional to the strength of the electron-phonon coupling.²³ With reasonable parameter values²³ and the combination of $t_0 = 0.9$ eV and $\lambda = 7.41$ eV/Å, the calculated spectra shown in Fig. 2(a) and the thick (blue) line in Fig. 2(b) closely resemble the experimental observations. The calculated RIXS response peaks near 2 eV, and increases rapidly as \mathbf{Q}_{2D} increases away from (0,0), towards (0.5,0.5), as seen in the experiments. We note that the calculated spectra in Fig. 2(a) suggest a slight dispersion of about 130 meV of the 2 eV peak. Such a small dispersion is below the detection limit of our experiment. We note however, that dispersion was reported in the related compound $\text{LaSr}_2\text{Mn}_2\text{O}_7$.¹⁹

The sensitivity of the RIXS response to intersite hopping and the electron-phonon coupling is shown in Fig. 2(b) by vary-

ing t_0 and λ .²³ For a given t_0 , λ is constrained such that the d - d excitation in the RIXS response peaks near 2 eV. Henceforth, only t_0 is mentioned for simplicity. The details of the combinations of t_0 and λ can be found in the Supplemental Material.²³ As was done for the experimental data, the calculated response is integrated over the same 1–3 eV window to generate the curves in Fig. 2(b), and again the value at $\mathbf{Q}_0 = (-0.03, -0.03)$ is subtracted. The calculated results show the best agreement with the experimental observations when $t_0 = 0.9$ eV. For larger t_0 values, the calculated RIXS response differs significantly from the experimental data. Thus our study sets the upper limit of t_0 . The inability to precisely determine the parameter values is largely due to the difficulty in determining the contributions from other inelastic scattering processes that give rise to a smooth “background” in the low energy loss region.

To further understand the implications of the observed momentum dependence of the RIXS spectrum for the screening dynamics, we calculate the real-space screening configurations from the lowest energy intermediate eigenstates. These are shown in the top panels of Fig. 3. Figures 3(a) and 3(b) compare the charge redistributions for $t_0 = 0.9$ and 1.5 eV, respectively, with the core hole at either a Mn^{3+} or a Mn^{4+} site. The volumes of the red and blue spheres scale with the screening electron and hole densities on the individual sites. For $t_0 = 0.9$ eV, the screening hole is tightly bound to the excited electron with more than 90% of the excited charge located on the three nearest-neighbor sites along the zigzag chain. For the large hopping parameter, $t_0 = 1.5$ eV, the screening pattern in real space changes drastically. The majority of the hole distribution in Fig. 3(b) is now beyond the nearest-neighbor sites, and is spread throughout the zigzag chains.

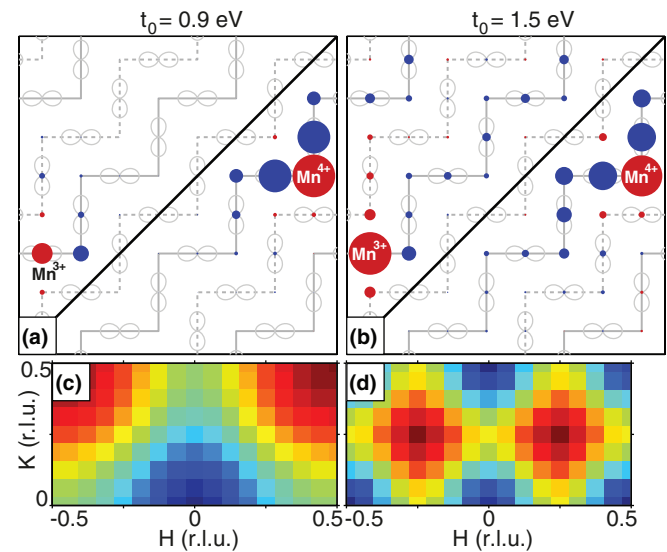


FIG. 3. (Color online) (a) and (b): Screening configuration in real space for $t_0 = 0.9$ and 1.5 eV, respectively. The top left half corresponds to the case with the core hole at a Mn^{3+} site, while the bottom right it is at a Mn^{4+} site. The volumes of the red and blue spheres are proportional to the electron and hole numbers. The large red spheres at Mn^{4+} core-hole sites represent about 0.9 electrons. (c) and (d): Integrated RIXS intensity plotted in the $(H, K, 0)$ plane of reciprocal space for $t_0 = 0.9$ and 1.5 eV, respectively. Red and blue represent the maximum and minimum intensities, respectively.

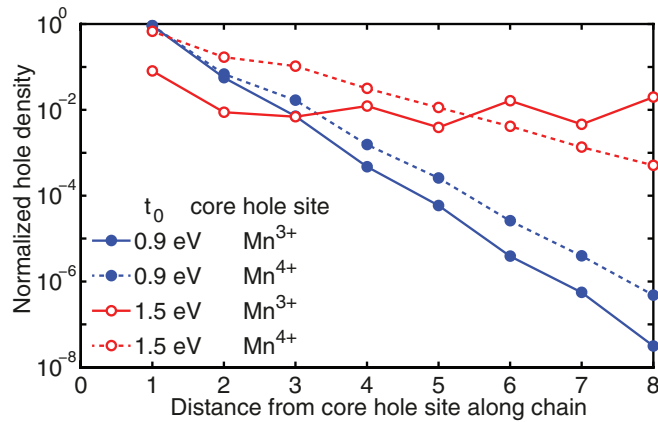


FIG. 4. (Color online) The excited hole number normalized by the excited electron number at the core-hole site, plotted in semilogarithmic scale with respect to the distance from the core-hole site along the zigzag chain.

This difference in screening dynamics is directly reflected in the RIXS response. Figures 3(c) and 3(d) show the calculated RIXS intensities for the two screening patterns over half of a Brillouin zone. When the screening hole is tightly bound to the excited electron for $t_0 = 0.9$ eV, the predominant wave vector for these electron and hole distributions is $(0.5, 0.5)$, coincident with the location of the RIXS peak intensity maximum in reciprocal space in Fig. 3(c) and in agreement with our experimental results. While for the much delocalized screening when $t_0 = 1.5$ eV, the maximum of the RIXS response is shifted to lower Q , as shown in Figs. 2(b) and 3(d). This RIXS response is completely at odds with the experiment results.

The charge redistribution for these two screening patterns is shown more clearly in Fig. 4, where the relative hole number at a given site is plotted as a function of the distance from the core-hole site, as measured along the zigzag chain. The semilogarithmic plot reveals an exponential decay of the hole density, confirming the presence of excitonlike screening clouds. The size of the screening cloud, which characterizes the screening dynamics and determines the RIXS response, depends strongly on the hopping strength t_0 . Taking the $t_0 = 0.9$ eV case, which best describes the RIXS data, we fit the excited hole distributions to an exponential function and find that the sizes of the screening clouds are 0.4 and 0.5 atomic spacings for the Mn^{3+} and Mn^{4+} sites, respectively.

$\text{La}_{0.5}\text{Sr}_{1.5}\text{MnO}_4$ was chosen for this study in part to take advantage of its particular one-dimensional (1D) nature in the low temperature ordered state, which helps to enhance the momentum dependence along the (H, H) direction and simplifies the analysis. However, we note that K -edge RIXS should be sensitive to the screening dynamics for all transition

metal oxides for which the bands near the Fermi energy are several electron volts in width. Indeed, momentum-dependent intensities were also observed in $\text{LaSr}_2\text{Mn}_2\text{O}_7$ which showed significant variation as a function of temperature across different phases.¹⁹ Most of the current studies on understanding dopant effects are still at the modeling and simulation stage in large part because of the lack of good experimental probes. In this study, we have shown that K -edge RIXS is a promising probe of the screening dynamics created in response to a localized potential. Importantly, the lifetime of a core hole is very short, typically on the order of femtoseconds. Thus the screening dynamics for this transient state is dominated by the electronic response since the ionic screening occurs on a much slower time scale (typically picoseconds). This allows the separation of the intrinsic electronic screening from that due to lattice distortions, the relative importance of which has been debated for years in the context of understanding nanoscale inhomogeneities in cuprates.^{3,24,25}

In summary, we observe a highly momentum-dependent K -edge resonant inelastic x-ray scattering intensity in the orbital ordered, layered manganite $\text{La}_{0.5}\text{Sr}_{1.5}\text{MnO}_4$. We interpret this through a comparison with calculations based on a tight-binding approach, and show that these observations imply a highly localized, nearest-neighbor screening of the local charge perturbation. We further find that the momentum dependence of the RIXS spectrum reflects the pattern and range of the screening in real space, and thus are able to measure the size and shape of the screening cloud. We find that the screening cloud is localized to a few Mn sites in the Mn-O plane, emphasizing the short-range nature of the Coulomb interactions in the manganites.

The work at Brookhaven was supported by the US Department of Energy, Division of Materials Science, under Contract No. DE-AC02-98CH10886. M.v.V. was supported by the US Department of Energy, Office of Basic Energy Sciences, Division of Materials Sciences and Engineering under Award No. DE-FG02-03ER46097 and NIU Institute for Nanoscience, Engineering, and Technology. The collaborations between T.F.S., K.H.A., and M.v.V. were supported by the Computational Materials and Chemical Science Network under Grants No. DE-FG02-08ER46540 and No. DE-SC0007091. K.H.A. is further supported by Argonne X-ray Science Division Visitor Program. Work at Argonne National Laboratory and use of the Advanced Photon Source was supported by the US DOE, Office of Science, Office of Basic Energy Sciences, under Contract No. DE-AC02-06CH11357. H.D. was supported by Grant No. 2010CB923000 from MOST, China. Work in Oxford was supported by the UK Engineering and Physical Sciences Research Council.

¹H. Alloul, J. Bobroff, M. Gabay, and P. J. Hirschfeld, *Rev. Mod. Phys.* **81**, 45 (2009).

²A. V. Balatsky, M. I. Salkola, and A. Rosengren, *Phys. Rev. B* **51**, 15547 (1995).

³K. McElroy, J. Lee, J. A. Slezak, D.-H. Lee, H. Eisaki, S. Uchida, and J. C. Davis, *Science* **309**, 1048 (2005).

⁴J. Zhang, Ismail, R. G. Moore, S.-C. Wang, H. Ding, R. Jin, D. Mandrus, and E. W. Plummer, *Phys. Rev. Lett.* **96**, 066401 (2006).

⁵J. Das, A. V. Mahajan, J. Bobroff, H. Alloul, F. Alet, and E. S. Sørensen, *Phys. Rev. B* **69**, 144404 (2004).

⁶G. D. Mahan, *Many-Particle Physics*, 2nd ed. (Plenum, New York, 1993).

- ⁷T. S. Nunner, B. M. Andersen, A. Melikyan, and P. J. Hirschfeld, *Phys. Rev. Lett.* **95**, 177003 (2005).
- ⁸A. T. Rømer, S. Graser, T. S. Nunner, P. J. Hirschfeld, and B. M. Andersen, *Phys. Rev. B* **86**, 054507 (2012).
- ⁹S. Zhou, H. Ding, and Z. Wang, *Phys. Rev. Lett.* **98**, 076401 (2007).
- ¹⁰Z. Wang, J. R. Engelbrecht, S. Wang, H. Ding, and S. H. Pan, *Phys. Rev. B* **65**, 064509 (2002).
- ¹¹L. J. P. Ament, M. van Veenendaal, T. P. Devereaux, J. P. Hill, and J. van den Brink, *Rev. Mod. Phys.* **83**, 705 (2011).
- ¹²K. H. Ahn, A. J. Fedro, and M. van Veenendaal, *Phys. Rev. B* **79**, 045103 (2009).
- ¹³J. van den Brink and M. van Veenendaal, *Europhys. Lett.* **73**, 121 (2006).
- ¹⁴J. Herrero-Martín, J. Blasco, J. García, G. Subías, and C. Mazzoli, *Phys. Rev. B* **83**, 184101 (2011).
- ¹⁵J. Bała and P. Horsch, *Phys. Rev. B* **72**, 012404 (2005); Y. S. Lee, S. Onoda, T. Arima, Y. Tokunaga, J. P. He, Y. Kaneko, N. Nagaosa, and Y. Tokura, *Phys. Rev. Lett.* **97**, 077203 (2006).
- ¹⁶Y. S. Lee *et al.*, *Phys. Rev. B* **75**, 144407 (2007).
- ¹⁷R. Kraus, M. Schrade, R. Schuster, M. Knupfer, A. Revcolevschi, B. Büchner, and J. Geck, *Phys. Rev. B* **83**, 165130 (2011).
- ¹⁸T. Inami *et al.*, *Phys. Rev. B* **67**, 045108 (2003); S. Grenier *et al.*, *Phys. Rev. Lett.* **94**, 047203 (2005).
- ¹⁹F. Weber, S. Rosenkranz, J. P. Castellán, R. Osborn, J. F. Mitchell, H. Zheng, D. Casa, J. H. Kim, and T. Gog, *Phys. Rev. B* **82**, 085105 (2010).
- ²⁰The elastic line was subtracted by using a model function. The latter was determined by measuring the elastic scattering at an off-resonant energy (7 eV below the edge), where there are negligible inelastic contributions.
- ²¹**Q** points such as (0,0,*L*), which would have been preferable, are intentionally avoided due to specular reflection enhancement of the elastic line at such points.
- ²²K. H. Ahn and A. J. Millis, *Phys. Rev. B* **61**, 13545 (2000).
- ²³See Supplemental Material at <http://link.aps.org/supplemental/10.1103/PhysRevB.87.201103> for the details of the Hamiltonian and its parameters.
- ²⁴K. Fujita, T. Noda, K. M. Kojima, H. Eisaki, and S. Uchida, *Phys. Rev. Lett.* **95**, 097006 (2005).
- ²⁵W. B. Gao, Q. Q. Liu, L. X. Yang, Y. Yu, F. Y. Li, C. Q. Jin, and S. Uchida, *Phys. Rev. B* **80**, 094523 (2009).